ACS OMEGA

Article

http://pubs.acs.org/journal/acsodf

Sol–Gel Synthesis of $CaTiO_3:Pr^{3+}$ Red Phosphors: Tailoring the Synthetic Parameters for Luminescent and Afterglow Applications

Daniela Meroni,*[,†,‡] Luca Porati,[†] Francesco Demartin,[†] and Dirk Poelman*[,§]

[†]Dipartimento di Chimica, Università degli Studi di Milano, Via Golgi 19, 20133 Milano, Italy

[‡]Consorzio Interuniversitario Nazionale per la Scienza e la Tecnologia dei Materiali (INSTM), Via Giusti 9, 50121 Firenze, Italy

[§]LumiLab, Department of Solid State Sciences, Ghent University, Krijgslaan 281, S1 9000 Ghent, Belgium

Supporting Information

ABSTRACT: Two sol–gel synthetic routes for the preparation of $CaTiO_3:Pr^{3+}$ red emitting phosphors were compared, with the aim of producing nanostructured materials with tailored luminescence/afterglow properties. The effect of the synthetic parameters, such as the addition of a stabilizer and calcination temperature, on the structural, morphological, and optical properties was investigated. The desired perovskite phase was obtained at a calcination temperature of 800 °C or higher. Although the use of acetic acid as the chelating agent leads to micrometric particles with heterogeneous composition, the presence of hydroxypropylcellulose (HPC) results in smaller, less aggregated particles as well as in a high phase purity. At the highest HPC content, surface Ca-rich impurities were detected, although no segregated Ca-rich phases were detectable by X-ray powder diffraction analyses. Luminescence properties were found to be positively related to the phase purity of the oxide, with the highest quantum yields at temperatures equal to or higher than 1000 °C. On the contrary, persistent luminescence properties were highest at intermediate calcination temperatures and for samples synthesized with acetic acid. Overall, a notable role of oxygen vacancies resulting from local Ca excess was observed, acting as trap levels promoting longer relaxation pathways. Thanks to the small-sized particles and best steady-state luminescent properties due to a substantial decrease of lattice defects, the HPC synthesis is a promising strategy for light-emitting diode applications. On the other hand, the acetic acid synthesis promoted a higher defect density, which is required for an efficient yield of light emission in the long time range and is thus more suitable for afterglow applications.

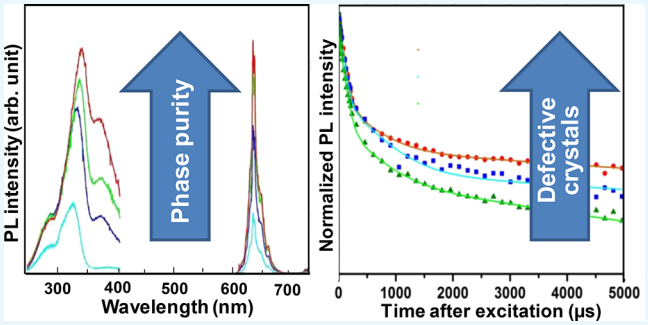

1. INTRODUCTION

Praseodymium-doped calcium titanate ($CaTiO_3:Pr^{3+}$) is a phosphor showing a red emission very close to the International Commission on Illumination coordinates of ideal red.[1] Furthermore, this compound has a high chemical and thermal stability, a good resistance to high-density electron irradiation, and its luminescence efficiency can be maintained under a prolonged flow of electric charge.[2,3] These properties make $CaTiO_3:Pr^{3+}$ a promising candidate to substitute currently available red luminescent materials in applications such as light-emitting diode (LED) displays, low-voltage field emission displays (FEDs), and plasma display panels.[4]

Furthermore, $CaTiO_3:Pr^{3+}$ belongs to the class of persistent phosphors, that is, materials exhibiting sustained light emission for an extended duration after removal of the light source. While materials with blue or green afterglow emission are relatively common, red persistent phosphors are quite rare. As a result, $CaTiO_3:Pr^{3+}$ represents a promising material for a broad range of applications, such as safety signage, sunlight storage, and bioimaging.[5]

Owing to the luminescence and afterglow properties of $CaTiO_3:Pr^{3+}$, a great deal of effort has been devoted to developing tailored synthetic routes of this material. A careful design of the synthetic procedure is crucial to either reduce the afterglow for display applications or, oppositely, to enhance the afterglow for application as persistent phosphors.[3,6] The most commonly reported synthetic procedures are based on solid-state reactions, especially for applications as luminescent materials.[7,8] Several other synthetic approaches for the synthesis of pure and doped $CaTiO_3$ have been reported, such as solvothermal,[9] hydrothermal,[10,11] electrospinning,[1] sputtering,[12] sonochemical,[2] and template synthesis.[13,14] However, not all of the reported procedures are able to provide at the same time a good degree of crystallinity and nanometric morphologies. In this respect, sol–gel syntheses present several advantages with respect to the more commonly employed solid-state reactions, for example, lower reaction temperatures, higher homogeneity of the final product, and smaller particles.[15] This latter aspect is favorable to applications

Received: June 9, 2017
Accepted: August 11, 2017
Published: August 28, 2017

DOI: 10.1021/acsomega.7b00761
ACS Omega 2017, 2, 4972–4981

in bioimaging as well as in displays like LED and FED, where smaller grain sizes may reduce charge accumulation.[16]

In this work, different sol−gel synthetic approaches for the synthesis of $CaTiO_3:Pr^{3+}$ phosphors are compared with the aim of controlling the particle morphology and tailoring the luminescence/afterglow properties for different applications. The two investigated approaches differ only for the type of species added to modulate crystal growth and agglomeration phenomena: a method in the presence of a chelating acid (acetic acid) as hydrolysis inhibitor and another method based on the addition of a polymer (hydroxypropylcellulose, HPC) as steric stabilizer. To the authors' best knowledge, these synthetic approaches have never been previously adopted for the preparation of phosphors based on $CaTiO_3$. The effect of the ensuing calcination step (in the range 600−1200 °C) is discussed in detail. The prepared samples were thoroughly characterized for their structural, morphological, optical, and luminescence properties. The duration of the luminescence after the removal of the light source was investigated by both luminescence decay measurements (studying short emission, in the microseconds range) and persistent luminescence measurements (long emission, in the order of minutes).

2. RESULTS AND DISCUSSION

2.1. Structural Features. X-ray powder diffraction (XRPD) measurements were carried out to identify the crystalline structure of each sample. Figures 1 and S1 present the XRPD patterns of Pr-doped and undoped samples, respectively. The standard pattern of orthorhombic perovskite $CaTiO_3$ is reported as a reference.

The $CaTiO_3:Pr^{3+}$ AA sample calcined at 600 °C (Figure 1a) shows an XRPD pattern characteristic of a crystalline sample, with calcite $CaCO_3$ as the main component and smaller amounts of other phases (anatase TiO_2, orthorhombic $CaTiO_3$, and CaO). On the contrary, the two samples synthesized with HPC and annealed at 600 °C (Figure 1b,c) show XRPD patterns characteristic of an essentially amorphous phase, as evidenced from the absence of well defined and intense peaks. This observation is supported also by photoluminescence measurements (vide infra). Similar to the doped sample, the undoped $CaTiO_3$ AA sample calcined at 600 °C is crystalline (Figure S1) and presents calcite $CaCO_3$ as main phase, with CaO and $CaTiO_3$ as minor components. Undoped samples from HPC synthesis are much less crystalline (Figure S1). This difference can be related to the presence of HPC, which has been reported to affect the phase composition of oxides synthesized via sol−gel reactions.[17]

Although all samples calcined at 800 °C present orthorhombic perovskite $CaTiO_3$ (ICDS 16688) as the main component, the two sets of syntheses are rather different. The AA_800 samples show orthorhombic $CaTiO_3$ as the main component and significant amounts of impurities, mainly $Ca(OH)_2$, rutile TiO_2, and $CaCO_3$, as clearly appreciable from Figure 1a. Both samples from HPC synthesis calcined at 800 °C instead are characterized by a higher phase purity.

In the samples annealed at 1000 and 1200 °C, all main peaks can be assigned to the orthorhombic perovskite $CaTiO_3$ phase, with rutile TiO_2 and $Ca(OH)_2$ as minor impurities, more appreciable in AA samples. The addition of HPC seems instead to promote the perovskite phase, leading in most cases to pure orthorhombic perovskite $CaTiO_3$. As expected due to the low dopant content adopted in this study (0.2%), XRPD patterns

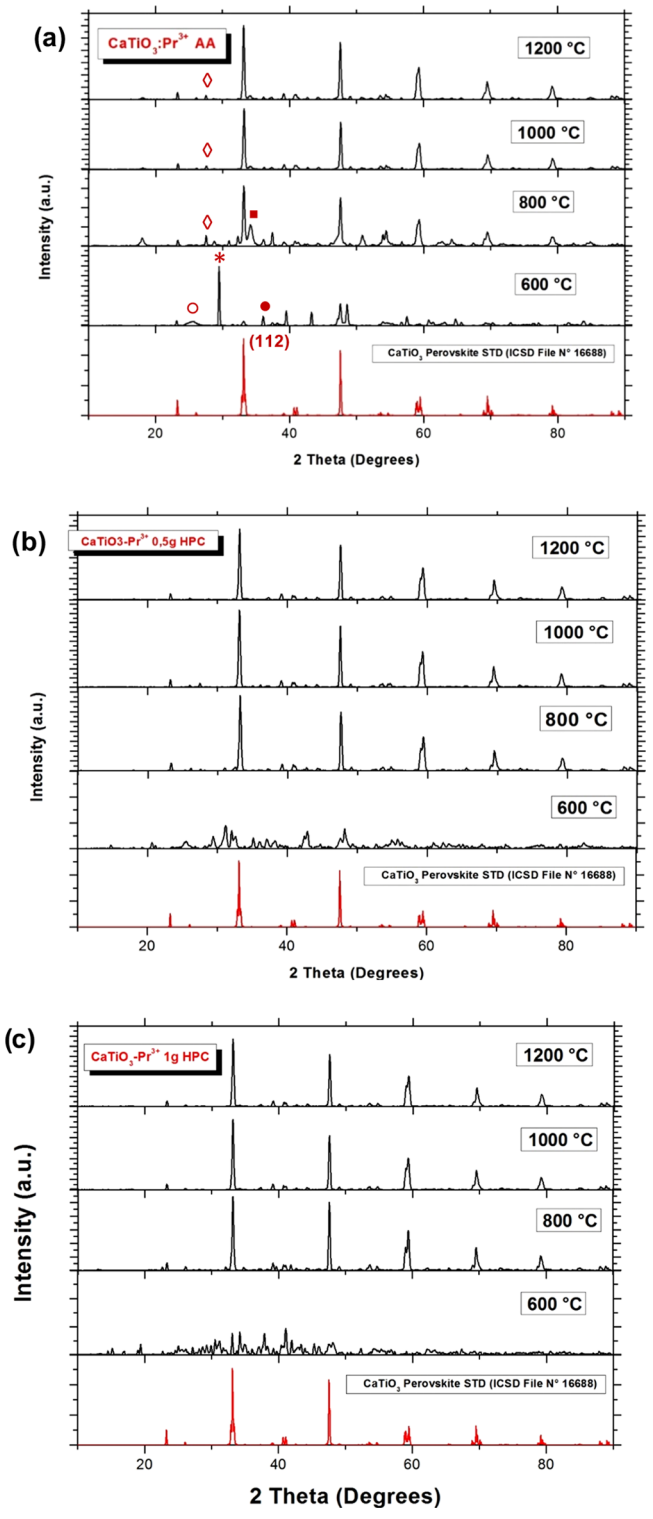

Figure 1. XRPD patterns of $CaTiO_3:Pr^{3+}$ samples calcined at different temperatures: (a) AA; (b) HPC 0.5 g; (c) HPC 1 g. The standard pattern of orthorhombic $CaTiO_3$ perovskite is reported as a reference, highlighting the most intense peak, (112). The main impurity peaks are also highlighted: $CaCO_3$ (star), $Ca(OH)_2$ (full square), CaO (full circle), anatase TiO_2 (empty circle), and rutile TiO_2 (diamond).

do not show consistent evidence of a shift in the (112) peak position in Pr-doped samples with respect to the undoped ones.

The obtained results are in good agreement with Fourier transform infrared (FTIR) spectra (Figure S2), showing the

DOI: 10.1021/acsomega.7b00761
ACS Omega 2017, 2, 4972−4981

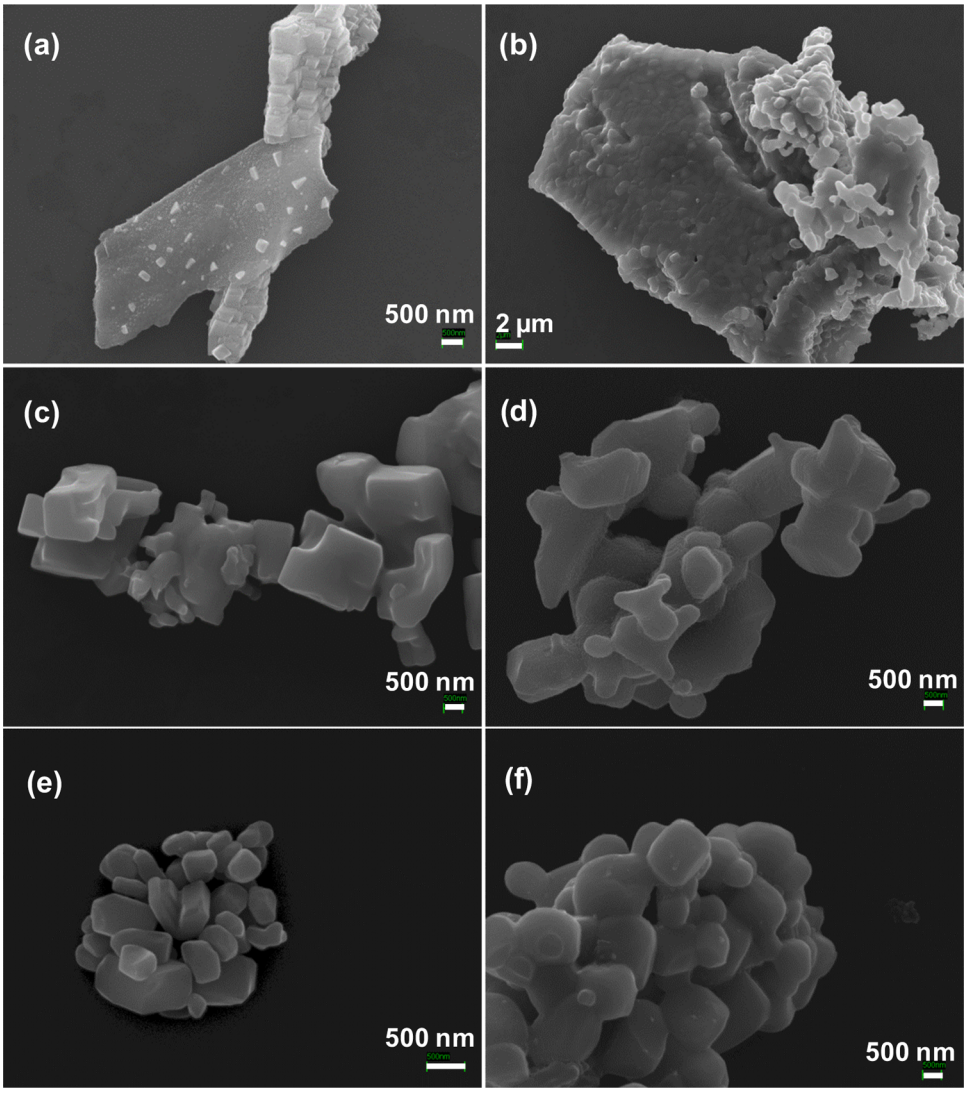

Figure 2. SEM images of $CaTiO_3:Pr^{3+}$ samples calcined at 800 (a, c, e) and 1200 °C (b, d, f): (a, b) AA, (c, d) HPC 0.5 g, and (e, f) HPC 1 g.

characteristic vibration modes of $CaTiO_3$ for all samples calcined above 600 °C: the peaks at ca. 530 and 420 cm^{-1} are associated with the vibrations of Ca−O bonds[18] and with the asymmetrical stretching vibration of the Ti−O bond in TiO_3^{2-} groups,[19] respectively. Other peaks are appreciable, especially at the lowest calcination temperatures. In the case of the AA series, the characteristic peaks of $CaCO_3$ calcite (713, 875, and 1410 cm^{-1}) are appreciable at 600 and 800 °C, in agreement with XRPD data. On the other hand, the HPC samples calcined at 600 and 800 °C present as the main feature a broad band at 2900−3700 cm^{-1}, characteristic of the stretching vibration of hydroxyl groups, with its bending counterpart at 1635 cm^{-1}. These HPC samples also present two peaks at 874 and 1439 cm^{-1}, which might be related to amorphous $CaCO_3$ on the grounds of the absence of the component at 710 cm^{-1} and in agreement with XRPD results. Increasing the calcination temperature leads to the appearance of peaks related to $Ca(OH)_2$ (3645, 1465, and 875 cm^{-1}) in the AA and HPC 1 g series. Interestingly, no peaks related to $Ca(OH)_2$ are appreciable for the HPC 0.5 g series, also in agreement with XRPD results showing only rutile TiO_2 as minor contaminant for both the undoped and doped samples of this series. It is interesting to note that FTIR was able to detect Ca-rich species also in samples whose XRPD patterns are consistent with those of pure orthorhombic $CaTiO_3$. Indeed local Ca excesses, such as isolated defects or grouping with irregular periodicity, might not be appreciable from XRPD analyses.[20]

2.2. Morphology and Elemental Composition. Figure 2 reports the scanning electron microscope (SEM) images of Pr-doped samples calcined at 800 and 1200 °C. Figure 2a shows that the AA_800 sample presents micrometric, flat agglomerates composed of sintered spherical particles that energy dispersive X-ray (EDX) mapping confirmed to be $CaTiO_3$. This sample is highly inhomogeneous, presenting also smaller and more porous aggregates (not shown) mainly composed of $CaO/Ca(OH)_2$. As appreciable from Figure 2b, increasing the calcination temperature seems to lead to larger agglomerates.

Samples obtained from the synthesis with HPC present a completely different and more homogeneous morphology (Figure 2c−f). Both samples are made of looser aggregates of polydispersed prismatic particles (Figure 2c,e). Although the HPC 0.5 g sample presents micrometric particles (Figure 2c), the sample synthesized with the highest HPC content is composed of much smaller aggregates of nanometric particles (Figure 2e). As a matter of fact, the addition of HPC to homogeneous sols has been reported to increase the surface

DOI: 10.1021/acsomega.7b00761
ACS Omega 2017, 2, 4972−4981

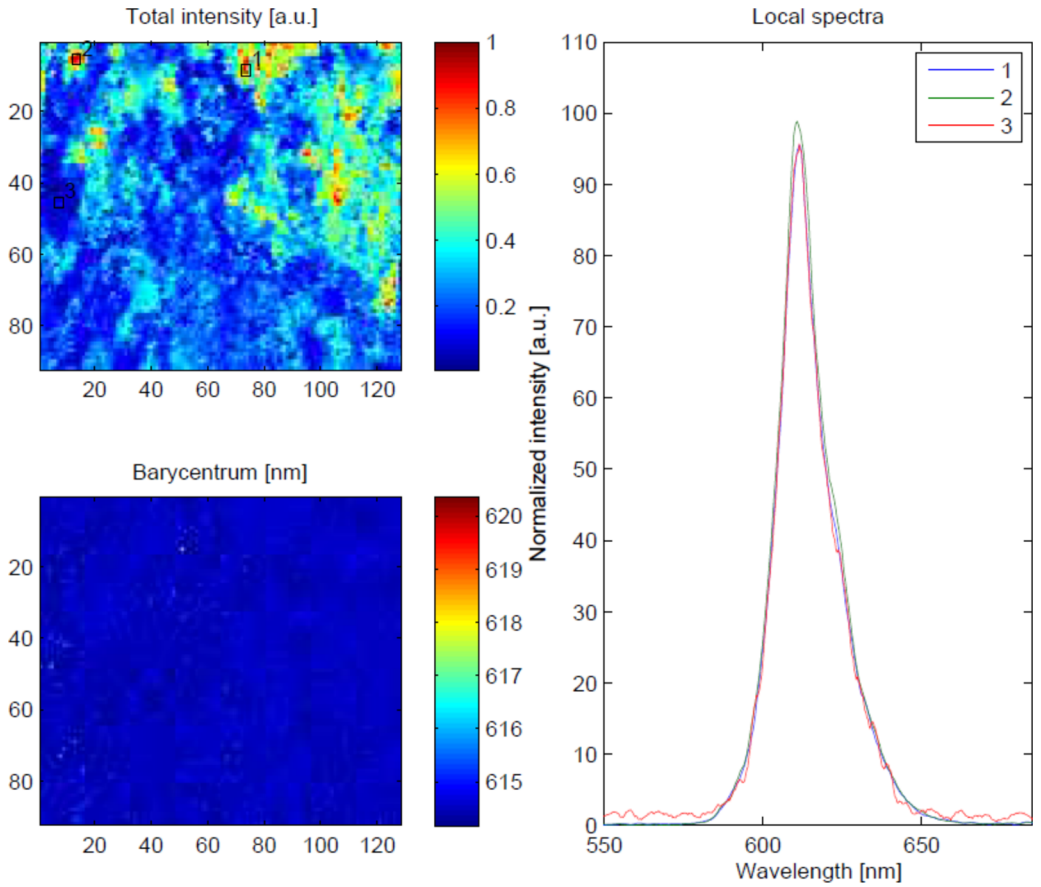

Figure 3. CL images representing the total intensity spectrum measured at the maximum emission wavelength, the barycenter and the local spectra of the $CaTiO_3:Pr^{3+}$ sample HPC 1 g _800. The relative SEM image is reported in Figure S3.

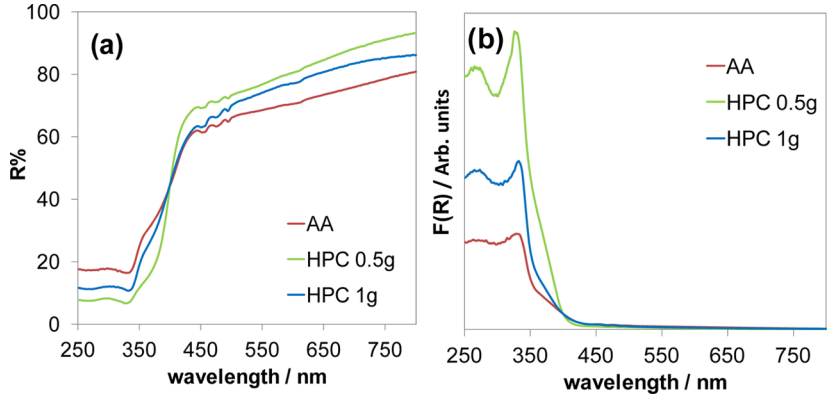

Figure 4. DRS spectra in reflectance (a) and Kubelka–Munk units (b) of $CaTiO_3:Pr^{3+}$ samples calcined at 1200 °C.

area of the final powder due to its ability to bind to the particle surface, preventing agglomeration between particles because of steric hindrance.[17,21,22] Interestingly, the effect of HPC on the sample morphology is appreciable even at a calcination temperature significantly higher than the degradation temperature of HPC, which occurs at around 400 °C.[23] Further increasing the annealing temperature leads to larger particles and sintering effects (Figure 2d,f).

EDX mapping (Figure S3c,d) shows that all of the elements (Ca, Ti, Pr, and O) are distributed homogeneously in the powders synthesized with HPC, within the detection limits of the EDX mapping. In the case of the AA sample, a less homogeneous composition is appreciable (Figure S3a,b), as also confirmed by spot analyses of different aggregates (vide supra). In all of the tested samples, no elemental impurities were detected. The average measured Ca/Ti atomic ratios are in agreement with nominal ones within experimental error. In the case of the $CaTiO_3:Pr^{3+}$ AA_800 sample, spot measurements detected areas with much lower Ti content, which may be indicative of impurity phases, as also supported by XRPD results (vide supra). A precise Pr quantification is difficult considering the low dopant nominal content (0.2%) due to the limits of the analytical technique.

Total intensity cathodoluminescence (CL) images of HPC samples show that the light is emitted homogeneously from the entire sample (Figure 3). Barycenter images display the

DOI: 10.1021/acsomega.7b00761
ACS Omega 2017, 2, 4972–4981

dominant wavelength of emission, which is, for each powder, constant throughout the sample. Local spectra compare the emission peaks detected in spots of the sample presenting a low and high emission intensity, respectively; they clearly show that the wavelength of emission is fully comparable also among areas of the sample showing different emission intensities. In the case of the AA sample calcined at 800 °C, CL mapping (Figure S4) reveals areas of very low emission intensity, which can be related to the poor homogeneity shown by XRPD and SEM-EDX results.

2.3. Optical Properties. The light absorption features of the undoped and doped samples were investigated by UV−vis diffuse reflectance spectroscopy (DRS) (Figure 4).

Figure 4 shows absorption features at 450−500 nm, which correspond to $^3H_4 \rightarrow {}^3P_J$ (J = 2, 1, 0) and $^3H_4 \rightarrow {}^1I_6$ transitions of Pr^{3+} ions.[24] The valence-to-conduction band edges are appreciable at ca. 335 nm. In addition, a shoulder at longer wavelength (band edge at about 375 nm) is observed, in agreement with previous reports.[25,26] Interestingly, the intensity ratio between the two absorption bands is different for the HPC 0.5 g sample with respect to AA and HPC 1 g. The origin of this band will be discussed in depth in Section 2.4.

The apparent band gap values, as determined by Tauc's plots assuming a direct band gap transition,[27] are reported in Table S1. They tend to decrease as a function of the annealing temperature. Calculated values for samples annealed above 800 °C are in the range 3.5−3.6 eV, fully comparable with the literature values for $CaTiO_3$.[27−29]

2.4. Photoluminescence (PL). Figure 5 reports the excitation and emission PL spectra measured at room temperature for each sample.

The shape of the excitation and emission peaks of the $CaTiO_3:Pr^{3+}$ AA samples does not vary by changing the annealing temperature, apart from a slight red shift of the excitation spectra. As for the samples synthesized with HPC, a different trend is observed. Although the peak shapes of samples annealed at 800, 1000, and 1200 °C are very similar, the samples obtained at 600 °C show an almost featureless excitation spectra, as expected due to their high amorphous content (see XRPD results).

All of the samples show a main excitation band at ca. 330 nm, which is consistent with the absorption edge of the diffuse reflectance spectra and can be attributed to the valence band to conduction band transition ($Ti^{4+}-O^{2-} \rightarrow Ti^{3+}-O^{-}$). Furthermore, an additional band at 280 nm is appreciable, which can be attributed to the lowest field component of the 5d state of Pr^{3+}.[30] In addition, both AA and HPC 1 g samples show an excitation peak at 380 nm (26 300 cm^{-1}), coincident with the shoulder observed in DRS spectra (Figure 4), which is generally assigned to a low-lying Pr-to-metal ($Pr^{3+}-Ti^{4+}$) intervalence charge-transfer state.[1,6] Interestingly, this peak is not appreciable in the excitation spectra of HPC 0.5 g samples. It is noteworthy that the apparent red shift of the main excitation peak of AA and HPC 1 g samples mirrors the progressive increase of the component at 380 nm. The relative intensity of the peak at 380 nm with respect to the one at 330 nm has been reported to depend on synthetic conditions, such as the calcination temperature,[30] deposition in film,[3] and local Ca excesses.[20] In particular, Otal and co-workers showed a progressive increase of the relative intensity of the peak at 380 nm with local Ca excess.[20] The relative intensity of the peaks depends in fact on the relative concentrations of Pr^{3+}, Pr^{4+}, and Ti^{3+} in the host $CaTiO_3$, which vary with the synthetic

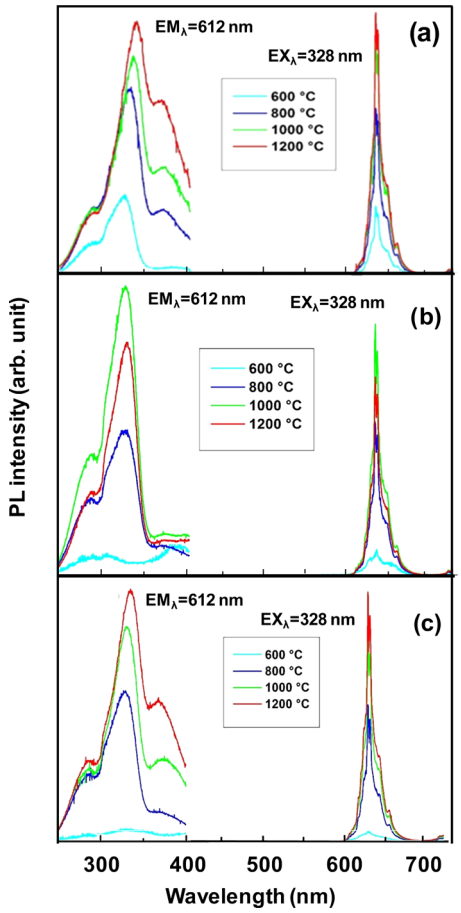

Figure 5. Excitation and emission spectra of $CaTiO_3:Pr^{3+}$ samples annealed at different temperatures: (a) AA, (b) HPC 0.5 g, and (c) HPC 1 g.

conditions.[30] It should be noted that with respect to HPC 0.5 g samples, the HPC 1 g and AA series showed appreciable impurities of Ca-rich phases, such as $Ca(OH)_2$ (see XRPD and FTIR results).

On the other hand, the shape of emission spectra is comparable for all of the samples. The peak at 628 nm can be attributed to $4f^2-4f^2$ transitions of Pr^{3+} ions from the excited state $^1D_2$ to the ground state $^3H_4$,[25,31] whereas the much less intense peak at 700 nm is due to $^1D_2-{}^3H_5$ transitions (Figure S5).

Table 1 reports the absolute PL quantum yield (QY) values of $CaTiO_3:Pr^{3+}$ samples calcined at 800, 1000, and 1200 °C.

Table 1. Absolute Quantum Yield Values for the Three Series of $CaTiO_3:Pr^{3+}$ Samples

sample	calcination temperature (°C)	QY (%)
AA	800	5.4
	1000	7.9
	1200	10.2
HPC 0.5 g	800	5.4
	1000	10.5
	1200	6.9
HPC 1 g	800	N.A.
	1000	10.5
	1200	9.7

DOI: 10.1021/acsomega.7b00761
ACS Omega 2017, 2, 4972−4981

Samples calcined at 600 °C were not analyzed due to their low PL intensity.

A marked difference is appreciable between the AA and HPC sample series. For AA samples, QY values increase monotonically as a function of the calcination temperature, reaching a maximum for the sample treated at 1200 °C. In the case of samples from the HPC synthesis, instead, the highest QY values are reached at the annealing temperature of 1000 °C. In the case of the AA series, the increase of QY with the calcination temperature can be related to the higher phase purity obtained at higher annealing temperatures. No similar trends can be observed for QY values of HPC samples, possibly because these samples show comparable $CaTiO_3$ phase content at the three investigated calcination temperatures and because of the occurrence of sintering effects at increasing calcination temperatures. The absolute QY of the top performing samples of the three series are quite comparable (ca. 10.5%), which are higher than that in the previous literature reports concerning $CaTiO_3$:Pr^{3+} micrometric materials with the same dopant content[19] and higher or comparable to other lanthanide-doped $CaTiO_3$ phosphors with same dopant amounts.[32,33] It should be noted that several factors influence the reliable evaluation of absolute QY values of powder samples, which are highly scattering materials. Absolute quantum yields can be determined by the integrated sphere method. However, several factors can affect the measurement, especially reabsorption effects,[34] which require a careful optimization of the measurement setup.[35]

2.5. Effect of Temperature on Photoluminescence. With the purpose of investigating the sample luminescence behavior at different temperatures, PL spectra of samples calcined at 1200 °C were measured in the −263/77 °C temperature range (Figures S6 and S7). PL spectra measured in the −263/−73 °C range are characterized by narrow peaks typical of the 4f−4f transitions in lanthanides, whereas, as expected, at higher temperatures, peaks become broader and less intense. Emission spectra recorded at low temperatures (−263 °C) show nine components, in agreement with the Stark splitting of $^1D_2$ and $^3H_4$ manifolds of the Pr^{3+} ion at low temperature.[3] Spectral shapes are similar among different samples, with the notable exception of the excitation spectra of HPC 0.5 g samples (vide supra), as particularly evident at −263 °C.

A temperature-dependent line broadening of emission transitions is expected due to the electron distribution in vibrational levels at thermal equilibrium. However, although thermal line broadening should decrease the peak height as a function of temperature, the total emission intensity should be instead independent of temperature unless thermal quenching of the emission occurs. In the present case, a temperature dependence of the total emission intensity was observed (Figure 6), in agreement with previous reports.[6,36] The increase in total emission intensity with temperature, observed especially for the HPC 0.5 g sample, might indicate that the electron transfer process is thermally activated. Above a certain temperature, thermal quenching effects become dominant for all samples. Figure 6 shows that the energy barrier for thermal quenching varies among the different samples: the maximum total emission is observed at −196 °C for the sample AA_1200, at −263 °C for HPC 1 g_1200, and at −123 °C for HPC 0.5 g_1200. This implies that the temperature dependence of luminescence can be controlled, for example, by changing the synthetic condition. Inaguma et al.[36] reported that the emission

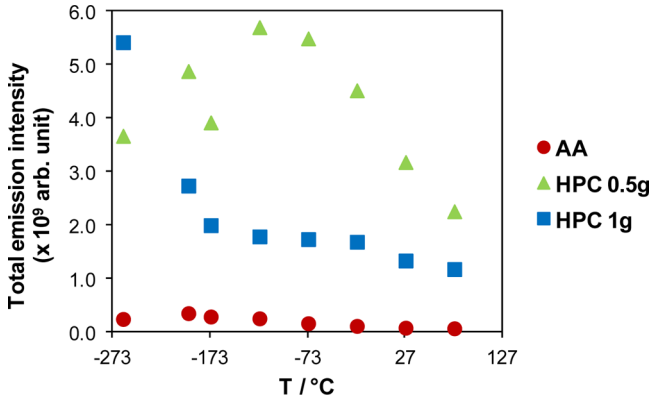

Figure 6. Total emission intensity (excitation at 328 nm) as a function of the measurement temperature for $CaTiO_3$:Pr^{3+} samples calcined at 1200 °C.

upon band gap excitation is promoted with increasing temperature and attributed this phenomenon to a thermally activated electron transfer from the ground state of Pr^{3+} ion, $^3H_4$, to the valence band. They instead observed a much more limited temperature dependence of emission intensity upon photoexcitation with a wavelength of 375 nm. Interestingly, the HPC 0.5 g sample, which lacks the excitation band at 375 nm, shows a higher activation energy from the $4f^n$ state to its crossover with the quenching state.

2.6. Luminescence Decay. Figure 7 compares the luminescence decay curves of $^1D_2$−$^3H_4$ transitions in samples

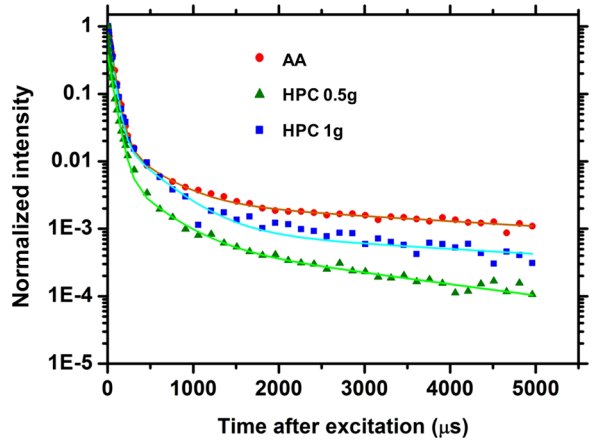

Figure 7. Luminescence decay curves of $^1D_2$−$^3H_4$ peaks of $CaTiO_3$:Pr^{3+} samples calcined at 1200 °C.

calcined at 1200 °C. The relative fitting parameters and the fraction of slow decay, f_3, are reported in Table 2.

For all samples, three exponential components turned out to be necessary for a good fit, revealing similar decay times for the different samples, of the order of 50 μs, 380 μs, and a few

Table 2. Decay Parameters of the $^1D_2$−$^3H_4$ Transition for $CaTiO_3$:Pr^{3+} Samples Calcined at 1200 °C

sample	I_1 (au)	τ_1 (μs)	I_2 (au)	τ_2 (μs)	I_3 (au)	τ_3 (μs)	f_3
AA	0.97	53	0.002	387	0.0026	5808	0.20
HPC 0.5 g	0.38	57	0.007	375	0.0007	2592	0.07
HPC 1 g	0.80	50	0.023	387	0.0010	5418	0.10

DOI: 10.1021/acsomega.7b00761
ACS Omega 2017, 2, 4972−4981

thousand microseconds. Different decay components of luminescent emission are typically reminiscent of dopants in different environments in the host lattice. The "slow" component in Table 2 should probably be interpreted as the first part of the afterglow; the fact that the "AA" sample has the largest fraction of slow decay nicely fits the fact that the afterglow is longest for this sample. The HPC 0.5 g sample shows the lowest f_3 value; these results are compatible with afterglow decay times (vide infra) and a possible explanation will be discussed in Section 2.7. Given the limited amount of data, only the orders of magnitude of the decay times in Table 2 should be trusted, and the absolute values should only be interpreted as approximations.

The effect of temperature on the luminescence decay was also investigated. Figure S8 compares the luminescence decay curves measured at −263 °C of $^1D_2$−$^3H_4$ peaks of $CaTiO_3$:Pr^{3+} samples calcined at 1200 °C. A faster decay was consistently observed at −263 °C than at room temperature (Table S2), in agreement with previous reports about $CaTiO_3$:Pr^{3+}.[37] The longer lifetimes observed at room temperature with respect to those at −263 °C can be considered the result of a thermal-activated process, involving charge storage from shallow surface traps.[37] This latter mechanism would be inefficient at low temperatures because of the deficiency of thermally released energy.

2.7. Afterglow Properties. Persistent luminescence emission spectra measured at room temperature (not shown) are consistent with photoluminescence, indicating that the afterglow results from the $^1D_2$−$^3H_4$ transition of Pr^{3+}. Figure 8 reports the afterglow decay curves of the three sets of samples.

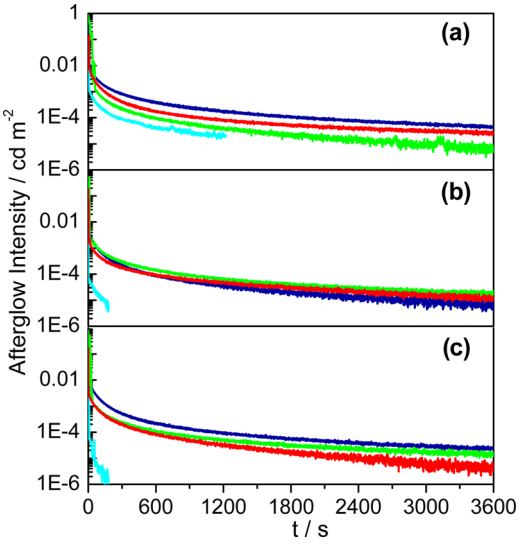

Figure 8. Afterglow decay curves of $CaTiO_3$:Pr^{3+} samples calcined at 600 (light blue line), 800 (blue), 1000 (green), and 1200 °C (red): (a) AA, (b) HPC 0.5 g, and (c) HPC 1 g.

At the annealing temperature of 600 °C, only the AA sample presents a limited afterglow, whereas the HPC samples do not show afterglow emission as expected on grounds of their amorphous nature.

All of the samples calcined at temperatures ≥800 °C present appreciable afterglow emission. The slowest decay of afterglow is observed for $CaTiO_3$:Pr^{3+} samples calcined at intermediate calcination temperatures: 800 °C (AA and HPC 1 g) and 1000 °C (HPC 0.5 g). These findings are also supported by the decay times of the phosphors (Table 3).

Table 3. Decay Times of Phosphor (Time until the Luminance Has Decayed to 0.32 mcd m^{-2}) for Different $CaTiO_3$:Pr^{3+} Samples

	t (s)		
calcination temperature (°C)	AA	HPC 0.5 g	HPC 1 g
600	92	3	9
800	737	221	442
1000	246	278	248
1200	374	155	199

The decay times of the phosphor for AA samples are generally higher than those of the other samples, whereas HPC 0.5 g samples presents the lowest. The highest decay time is shown by the AA_800 phosphor, which presents a decay time higher than that in previous literature reports.[20,38] It is worth noting that AA samples have the highest content of impurity phases, in particular Ca-rich ones, whereas HPC 0.5 g samples consistently showed the absence of Ca excess. The presence of local Ca excess has been related to the favored formation of oxygen vacancies that are known to act as charge-carrier traps, increasing decay times.[6,20,30] This supports the observation that the ideal preparation conditions for a phosphor strongly depend on the area of application: to improve the steady-state luminescence, the number of defects should be minimized, whereas such defects are essential for obtaining a high afterglow time and intensity.

Figure 9 compares the total light output of the different samples. The total light output in the entire investigated range (from 10 to 3600 s, Figure 9a) is compared with the slow afterglow (100−3600 s, Figure 9b).

The trend of the slow afterglow (Figure 9b) is different from the total light output in the entire range (Figure 9a). As a matter of fact, the highest total light output in Figure 9a is shown by the sample AA_1000, whereas in the slow afterglow (100−3600 s), it is shown by AA_800. Such a difference shows that for the sample calcined at 1000 °C, almost all of the light comes out in the first few minutes, possibly as a result of shallower traps.

The fact that the optimum annealing temperature for the afterglow properties of the AA series is 800 °C, whereas it is 1200 °C for steady-state luminescence, can be attributed to a competition between two effects: on one hand, a higher processing temperature leads to a better phase purity, which enhances the luminescent intensity and decreases nonradiative recombination. On the other hand, the afterglow is dependent on the existence of some intrinsic electronic and/or structural defects, which are decreasing in number with higher annealing temperatures. The persistent luminescence intensity is proportional to the number of traps for energy storage and to the recombination efficiency of the released carriers with luminescent centers. The nature of energy storage trapping centers in $CaTiO_3$:Pr^{3+} has been attributed to different mechanisms; the Pr^{3+} dopant itself acts as a hole trap and Pr^{4+} and oxygen vacancies as electron-traps.[6,30] The highest persistent luminescence intensity is observed for the samples prepared at 800 °C, owing to the high number of defects promoting afterglow. A further increase in the calcination temperature reduces the impurity content, in particular of Ca-

DOI: 10.1021/acsomega.7b00761
ACS Omega 2017, 2, 4972−4981

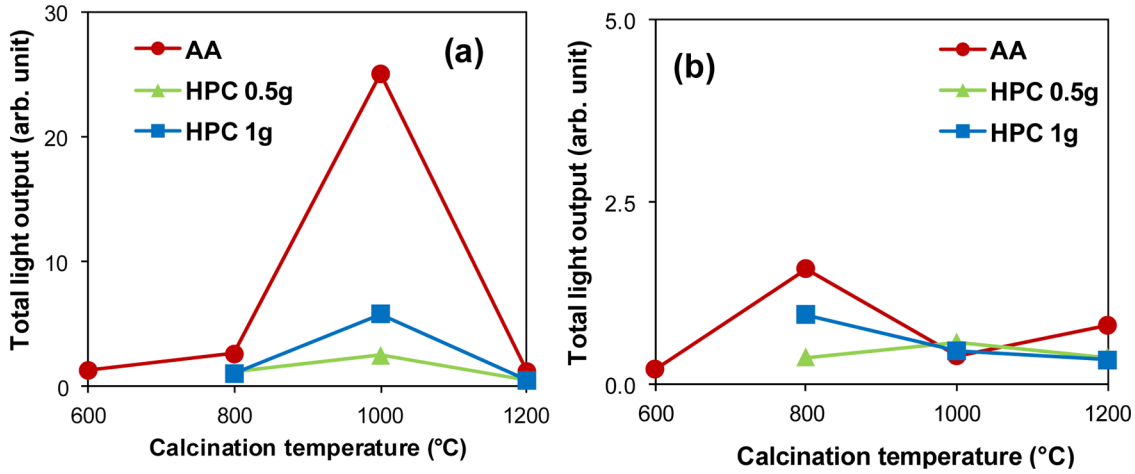

Figure 9. Total light output during afterglow measurements of $CaTiO_3:Pr^{3+}$ samples as a function their calcination temperature: (a) light emission from 10 to 3600 s (total afterglow) and (b) light emission from 100 to 3600 s (slow afterglow).

rich phases, which might result in a loss of oxygen vacancies.[39] As a result, the afterglow emission is reduced.

The calcination temperature has a strong influence on the afterglow properties of sample $CaTiO_3:Pr^{3+}$ AA and a lower influence on the samples synthesized with HPC, mirroring the diverse effect of calcination temperature on phase purity for the two sets of samples. Further, the samples synthesized with acetic acid showed values of total light output higher than those of the samples synthesized with HPC (also in agreement with decay times of the phosphors). This higher persistent luminescence might be the result of more defective crystals for samples of the AA series, related to their higher content of Ca-rich phases and local Ca excess.

3. CONCLUSIONS

In this work, two sol−gel synthetic routes for the preparation of $CaTiO_3:Pr^{3+}$ were developed. The role of the calcination temperature on the material properties was investigated in a wide temperature range (600−1200 °C). The desired perovskite phase was obtained at a calcination temperature of 800 °C or higher. The presence of HPC, able to adsorb at the oxide surface reducing coalescence via enhanced steric hindrance, results in smaller, less aggregated particles as well as in a high phase purity. The AA synthesis instead leads to micrometric particles with heterogeneous composition. The role of the HPC content was also investigated, showing that increasing the HPC content further reduces the particle size and agglomeration. Interestingly, the sample with the highest HPC content shows the presence of Ca-rich impurities, as determined by attenuated total reflection Fourier transform infrared (ATR-FTIR) analyses; although no segregated Ca-rich phases were appreciable from XRPD analyses, these effects might be traced back to a higher presence of surface defects in this sample. PL measurements showed that luminescence properties are mainly related to the phase purity of the oxide. The presence of Ca excess, resulting in oxygen vacancies, was related to effects on the samples' absorption and excitation spectra. On the other hand, a more complex effect was found on persistent luminescence properties. Although the samples calcined at the lowest temperature showed a negligible afterglow emission, the highest energy storage capability was exhibited by the $CaTiO_3:Pr^{3+}$ AA sample calcined at 800 °C. This indicates that a good degree of crystallization is needed for both steady-state PL and afterglow. However, annealing at 1200 °C leads to a diffusion degree that is too high for the afterglow phenomenon to occur. As a matter of fact, persistent luminescence requires the presence of trap levels, which are related to lattice defects, such as oxygen vacancies. The synthetic procedure played a significant role in the afterglow emission: samples from the synthesis with acetic acid showed the highest persistent luminescence, possibly as a result of the presence of local Ca excess, whereas the HPC 0.5 g samples showed the lowest afterglow.

Therefore, samples from the acetic acid synthesis are better candidates as red persistent phosphors. On the other hand, considering their high luminescent emission, low afterglow, and smaller particles, samples from HPC synthesis may be considered the most promising red phosphors for display applications.

4. EXPERIMENTAL METHODS

4.1. Materials Synthesis. Reagents were of analytical grade; they were purchased from Sigma-Aldrich and used without further purification. MilliQ water was used to prepare solutions and suspensions.

$CaTiO_3:Pr^{3+}$ powders were synthesized by the sol−gel method, followed by calcination at different temperatures. Two different synthetic procedures were compared: an acetic acid-based route and an HPC-based route. In both synthetic approaches, the precursor materials were $CaCO_3$, titanium tetraisopropoxide (TTIP) and $PrCl_3$. The Pr/Ti molar ratio was fixed to 0.2% to limit concentration quenching effects.[31] Undoped $CaTiO_3$ samples were also synthesized as reference. The general procedure was the following: 3.7 mL of a 0.02 M $PrCl_3$ acidic solution (prepared in HCl 0.1 M) was added to 10.84 g of TTIP while stirring continuously and using an ice bath. Then, 11.52 g of 2-propanol was added, leading to the formation of a transparent sol. Subsequently, a $CaCO_3$ solution was added drop-by-drop to the reaction mixture in 30 min. The reaction mixture was then stirred for 90 min and dried in an oven for 24 h at 70 °C. The obtained xerogels were calcined at different temperatures (600, 800, 1000, and 1200 °C) for 4 h in an unventilated oven, using a 3.3 °C min^{-1} heating rate.

The two synthetic approaches differed only in the preparation of the $CaCO_3$ solution. In the acetic acid-based approach, 3.72 g of $CaCO_3$ were mixed with 10.52 g of glacial

DOI: 10.1021/acsomega.7b00761
ACS Omega 2017, 2, 4972−4981

acetic acid. In the HPC-based approach, 3.72 g of $CaCO_3$ was added to an aqueous HPC solution, prepared dissolving the chosen amount of HPC ($M_W \sim 100\,000$) in 66.6 mL of water, and ca. 10 mL of HCl (37%) was introduced to obtain a clear solution. To investigate the effect of the HPC content on the final properties of the $CaTiO_3$ material, two different amounts of HPC were tested (1 and 0.5 g).

In the following, samples will be labeled as AA_*x*, HPC 1 g_*x* and HPC 0.5 g_*x*, where *x* is the calcination temperature.

4.2. Characterization Techniques. X-ray powder diffraction (XRPD) patterns were acquired at room temperature using a Siemens D5000 Bragg-Brentano goniometer graphite-monochromated Cu Kα radiation (λ = 0.15406 nm) at 40 kV × 40 mA nominal X-rays power. θ:2θ scans were performed between 10 to 90°, with step sizes 0.01−0.04° wide.

Fourier transform infrared (FTIR) spectroscopy measurements were carried out using a PerkinElmer Spectrum 100 ATR-FTIR spectrometer.

Scanning electron microscope (SEM) images were acquired with a Zeiss LEO 1430 (30 keV), equipped with a backscattered electron detector as well as an energy dispersive X-ray (EDX) analysis system. Specimens were coated with an Au thin film to reduce charging effects.

Cathodoluminescence (CL) and EDX mapping images were collected with a Hitachi S3400N scanning electron microscope operating at 15 kV, equipped with an optical fiber, and analyzed using an EMCCD camera (Princeton Instruments ProEM 1600[2]) attached to a Princeton Instruments Acton SP2358 spectrograph.

Diffuse reflectance spectroscopy (DRS) analyses were performed on a Shimadzu UV2600 UV−vis spectrophotometer equipped with an integrating sphere. Spectra were acquired in the range of 250−750 nm, using $BaSO_4$ as a total white reference. Band gap values were estimated by Tauc's plots.[40]

Photoluminescence (PL) measurements were performed using an FS920 fluorescence spectrometer (Edinburgh Instruments). Measurements at different temperatures were carried out using an Oxford Optistat CF cryostat. The total emission intensity was measured using the same setup of PL measurements, keeping the same geometry during every measurement and integrating the spectra over the 550−700 nm wavelength range.

Absolute PL quantum yield determinations were carried out with a Quantaurus-QY spectrometer (Hamamatsu), equipped with an integrating sphere. Samples were placed in optical quartz cells, used as reference. Excitation wavelengths were varied in the range of 230−360 nm (10 nm for each measurement); the maximum QY values were always determined in the 320−330 nm range. The emitted fluorescence in the range of 580−750 nm was detected by a multichannel detector. Measurements were performed at room temperature, according to a previously reported experimental setup.[41]

Luminescence decay measurements were conducted with an Intensified Charge Coupled Device (ICCD) Andor DH720 at two different temperatures (room temperature and −263 °C) by using an Oxford Optistat CF cryostat. Excitation was performed using a pulsed nitrogen laser (wavelength 337 nm, pulse duration <1 ns, pulse frequency 1 Hz), and detection was carried out at 612 nm. The response time of the detection system was determined by the laser pulse width and the switching time of the ICCD image intensifier (3 ns), leading to an overall response time of less than 5 ns, which is orders of magnitude below the time scale of the observed phenomena. After noise removal, the peaks of the different transitions were integrated and the decay curve was fitted as a function of time *t* by a triple exponential

$$I(t) = I_1\, e^{-t/\tau_1} + I_2\, e^{-t/\tau_2} + I_3\, e^{-t/\tau_3} \quad (1)$$

where I is the luminescence intensity, I_1, I_2, and I_3 are the amplitudes for each component, and τ_1, τ_2, and τ_3 are the decay constants of the three components, respectively. From the determined amplitudes and decay constants, the fraction of slow decay, f_3, was determined according to the following equation

$$f_3 = \frac{I_3\tau_3}{I_1\tau_1 + I_2\tau_2 + I_3\tau_3} \quad (2)$$

The persistent luminescence analysis was conducted by irradiating the sample with an unfiltered 150 W short arc xenon lamp (LOT Quantum Devices) at an illumination intensity of 1000 lx for 5 min and then measuring its afterglow emission for 1 h with an International Light Technology ILT1700 photometer, equipped with an SPM68 detector calibrated in cd m^{-2}. The decay time of the phosphor was determined as the time in which its emission decays to 0.32 mcd m^{-2} (3.2×10^{-4} cd m^{-2}).

■ ASSOCIATED CONTENT

Supporting Information

The Supporting Information is available free of charge on the ACS Publications website at DOI: 10.1021/acsomega.7b00761.

XRPD patterns of undoped samples; FTIR spectra of the $CaTiO_3$:Pr^{3+} samples; EDX mapping and CL images of selected samples; band gap values of doped and undoped samples; emission and excitation PL spectra of $CaTiO_3$:Pr^{3+} samples at different measuring temperatures; luminescence decay curves at −263 °C and relative fitting parameters (PDF)

■ AUTHOR INFORMATION

Corresponding Authors

*E-mail: daniela.meroni@unimi.it (D.M.).

*E-mail: dirk.poelman@ugent.be (D.P.).

ORCID

Daniela Meroni: 0000-0002-3386-9293

Notes

The authors declare no competing financial interest.

■ ACKNOWLEDGMENTS

Daniele Marinotto (University of Milan) is kindly acknowledged for support during quantum yield measurements. L.P. acknowledges financial support from the ERASMUS project.

■ REFERENCES

(1) Dong, G.; Xiao, X.; Zhang, L.; Ma, Z.; Bao, X.; Peng, M.; Zhang, Q.; Qiu, J. Preparation and Optical Properties of Red, Green and Blue Afterglow Electrospun Nanofibers. *J. Mater. Chem.* **2011**, *21*, 2194−2203.

(2) Alammar, T.; Hamm, I.; Wark, M.; Mudring, A.-V. Low-Temperature Route to Metal Titanate Perovskite Nanoparticles for Photocatalytic Applications. *Appl. Catal., B* **2015**, *178*, 20−28.

(3) Boutinaud, P.; Pinel, E.; Mahiou, R. Luminescence and Afterglow in $CaTiO_3$:Pr^{3+} Films Deposited by Spray Pyrolysis. *Opt. Mater.* **2008**, *30*, 1033−1038.

DOI: 10.1021/acsomega.7b00761
ACS Omega 2017, 2, 4972−4981

(4) Takashima, H.; Shimada, K.; Miura, N.; Katsumata, T.; Inaguma, Y.; Ueda, K.; Itoh, M. Low-Driving-Voltage Electroluminescence in Perovskite Films. *Adv. Mater.* **2009**, *21*, 3699−3702.
(5) Smet, P. F.; Van den Eeckhout, K.; De Clercq, O. Q.; Poelman, D. Persistent Phosphors. In *Handbook on the Physics and Chemistry of Rare Earths*; Bunzli, J.-C., Pecharsky, V. K., Eds.; North-Holland: Amsterdam, The Netherlands, 2015; pp 1−108.
(6) Boutinaud, P.; Sarakha, L.; Cavalli, E.; Bettinelli, M.; Dorenbos, P.; Mahiou, R. About Red Afterglow in Pr^{3+} Doped Titanate Perovskites. *J. Phys. D: Appl. Phys.* **2009**, *42*, No. 045106.
(7) Li, Y.; Gecevicius, M.; Qiu, J. Long Persistent Phosphors-from Fundamentals to Applications. *Chem. Soc. Rev.* **2016**, *45*, 2090−2136.
(8) Kaur, J.; Dubey, V.; Parganiha, Y.; Singh, D.; Suryanarayana, N. S. Review of the Preparation, Characterization, and Luminescence Properties of Pr^{3+}-Doped $CaTiO_3$ Phosphors. *Res. Chem. Intermed.* **2015**, *41*, 3597−3621.
(9) Yang, X.; Fu, J.; Jin, C.; Chen, J.; Liang, C.; Wu, M.; Zhou, W. Formation Mechanism of $CaTiO_3$ Hollow Crystals with Different Microstructures. *J. Am. Chem. Soc.* **2010**, *132*, 14279−14287.
(10) Dong, W.; Li, B.; Li, Y.; Wang, X.; An, L.; Li, C.; Chen, B.; Wang, G.; Shi, Z. General Approach to Well-Defined Perovskite $MTiO_3$(M = Ba, Sr, Ca, and Mg) Nanostructures. *J. Phys. Chem. C* **2011**, *115*, 3918−3925.
(11) Zhuang, J.; Tian, Q.; Lin, S.; Yang, W.; Chen, L.; Liu, P. Precursor Morphology-Controlled Formation of Perovskites $CaTiO_3$ and Their Photo-Activity for As(III) Removal. *Appl. Catal., B* **2014**, *156−157*, 108−115.
(12) Krause, A.; Weber, W. M.; Pohl, D.; Rellinghaus, B.; Verheijen, M.; Mikolajick, T. Investigation of Embedded Perovskite Nanoparticles for Enhanced Capacitor Permittivities. *ACS Appl. Mater. Interfaces* **2014**, *6*, 19737−19743.
(13) Demirörs, A. F.; Imhof, A. $BaTiO_3$, $SrTiO_3$, $CaTiO_3$, and $Ba_xSr_{1-X}TiO_3$ particles: A General Approach for Monodisperse Colloidal Perovskites. *Chem. Mater.* **2009**, *21*, 3002−3007.
(14) Pan, J. H.; Shen, C.; Ivanova, I.; Zhou, N.; Wang, X.; Tan, W. C.; Xu, Q.-H.; Bahnemann, D. W.; Wang, Q. Self-Template Synthesis of Porous Perovskite Titanate Solid and Hollow Submicrospheres for Photocatalytic Oxygen Evolution and Mesoscopic Solar Cells. *ACS Appl. Mater. Interfaces* **2015**, *7*, 14859−14869.
(15) Meroni, D.; Ardizzone, S.; Cappelletti, G.; Oliva, C.; Ceotto, M.; Poelman, D.; Poelman, H. Photocatalytic Removal of Ethanol and Acetaldehyde by N-Promoted TiO_2 Films: The Role of the Different Nitrogen Sources. *Catal. Today* **2011**, *161*, 169−174.
(16) Zhang, N.; Guo, C.; Zheng, J.; Su, X.; Zhao, J. Synthesis, Electronic Structures and Luminescent Properties of Eu^{3+} Doped $KGdTiO_4$. *J. Mater. Chem. C* **2014**, *2*, 3988−3994.
(17) Shukla, S.; Seal, S.; Vanfleet, R. Sol-Gel Synthesis and Phase Evolution Behavior of Sterically Stabilized Nanocrystalline Zirconia. *J. Sol-Gel Sci. Technol.* **2003**, *27*, 119−136.
(18) Lozano-Sánchez, L. M.; Lee, S.-W.; Sekino, T.; Rodríguez-González, V. Practical Microwave-Induced Hydrothermal Synthesis of Rectangular Prism-Like $CaTiO_3$. *CrystEngComm* **2013**, *15*, 2359.
(19) Peng, C.; Hou, Z.; Zhang, C.; Li, G.; Lian, H.; Cheng, Z.; Lin, J. Synthesis and Luminescent Properties of $CaTiO_3$: Pr^{3+} Microfibers Prepared by Electrospinning Method. *Opt. Express* **2010**, *18*, 7543−7553.
(20) Otal, E. H.; Maegli, A. E.; Vogel-Schäuble, N.; Walfort, B.; Hagemann, H.; Yoon, S.; Zeller, A.; Weidenkaff, A. The Influence of Defects Formed by Ca Excess and Thermal Post-Treatments on the Persistent Luminescence of $CaTiO_3$:Pr. *Opt. Mater. Express* **2012**, *2*, 405−412.
(21) Mohammadi, M. R.; Cordero-Cabrera, M. C.; Fray, D. J.; Ghorbani, M. Preparation of High Surface Area Titania (TiO_2) Films and Powders Using Particulate Sol−Gel Route Aided by Polymeric Fugitive Agents. *Sens. Actuators, B* **2006**, *120*, 86−95.
(22) Jean, J. H.; Ring, T. A. Effect of a Sterically Stabilizing Surfactant on the Nucleation, Growth and Agglomeration of Monosized Ceramic Powders. *Colloids Surf.* **1988**, *29*, 273−291.
(23) Huang, Y.; Kang, H.; Li, G.; Wang, C.; Huang, Y.; Liu, R. Synthesis and Photosensitivity of Azobenzene Functionalized Hydroxypropylcellulose. *RSC Adv.* **2013**, *3*, 15909−15916.
(24) Boutinaud, P.; Pinel, E.; Dubois, M.; Vink, A. P.; Mahiou, R. UV-to-Red Relaxation Pathways in $CaTiO_3$:Pr^{3+}. *J. Lumin.* **2005**, *111*, 69−80.
(25) Kyômen, T.; Sakamoto, R.; Sakamoto, N.; Kunugi, S.; Itoh, M. Photoluminescence Properties of Pr-Doped (Ca,Sr,Ba)TiO_3. *Chem. Mater.* **2005**, *17*, 3200−3204.
(26) Diallo, P. T.; Jeanlouis, K.; Boutinaud, P.; Mahiou, R.; Cousseins, J. C. Improvement of the Optical Performances of Pr^{3+} in $CaTiO_3$. *J. Alloys Compd.* **2001**, *323−324*, 218−222.
(27) Moreira, M. L.; Paris, E. C.; do Nascimento, G. S.; Longo, V. M.; Sambrano, J. R.; Mastelaro, V. R.; Bernardi, M. I. B.; Andrés, J.; Varela, J. A.; Longo, E. Structural and Optical Properties of $CaTiO_3$ Perovskite-Based Materials Obtained by Microwave-Assisted Hydrothermal Synthesis: An Experimental and Theoretical Insight. *Acta Mater.* **2009**, *57*, 5174−5185.
(28) Cavalcante, L. S.; Marques, V. S.; Sczancoski, J. C.; Escote, M. T.; Joya, M. R.; Varela, J. A.; Santos, M. R. M. C.; Pizani, P. S.; Longo, E. Synthesis, Structural Refinement and Optical Behavior of $CaTiO_3$ Powders: A Comparative Study of Processing in Different Furnaces. *Chem. Eng. J.* **2008**, *143*, 299−307.
(29) Katayama, Y.; Ueda, J.; Tanabe, S. Photo-Electronic Properties and Persistent Luminescence in Pr^{3+} Doped (Ca,Sr)TiO_3 Ceramics. *J. Lumin.* **2014**, *148*, 290−295.
(30) Jia, W.; Jia, D.; Rodriguez, T.; Evans, D. R.; Meltzer, R. S.; Yen, W. M. UV Excitation and Trapping Centers in $CaTiO_3$:Pr^{3+}. *J. Lumin.* **2006**, *119−120*, 13−18.
(31) Boutinaud, P.; Mahiou, R.; Cavalli, E.; Bettinelli, M. Red Luminescence Induced by Intervalence Charge Transfer in Pr^{3+}-Doped Compounds. *J. Lumin.* **2007**, *122−123*, 430−433.
(32) Xu, X.; Tang, Y.; Mo, F.; Zhoun, L.; Li, B. Synthesis and luminescent properties of $CaTiO_3$:Eu^{3+}, Al^{3+} phosphors. *Ceram. Int.* **2014**, *40*, 10887−10892.
(33) Wu, Y.-F.; Nien, Y.-T.; Wang, Y.-J.; Chen, I.-G. Enhancement of Photoluminescence and Color Purity of $CaTiO_3$:Eu Phosphor by Li Doping. *J. Am. Ceram. Soc.* **2012**, *95*, 1360−1366.
(34) Würth, C.; Geißler, D.; Behnke, T.; Kaiser, M.; Resch-Genger, U. Critical review of the determination of photoluminescence quantum yields of luminescent reporters. *Anal. Bioanal. Chem.* **2015**, *407*, 59−78.
(35) de Mello, J. C.; Wittmann, H. F.; Friend, R. H. An improved experimental determination of external photoluminescence quantum efficiency. *Adv. Mater.* **1997**, *9*, 230−232.
(36) Inaguma, Y.; Tsuchiya, T.; Mori, Y.; Imade, Y.; Sato, N.; Katsumata, T.; Mori, D. Temperature Dependence of Luminescence Properties of Praseodymium-Doped Perovskite $CaTiO_3$:Pr^{3+}. *Thermochim. Acta* **2012**, *532*, 168−171.
(37) Zhang, X.; Zhang, J.; Zhang, X.; Wang, M.; Zhao, H.; Lu, S.; Wang, X.-j. Size Manipulated Photoluminescence and Phosphorescence in $CaTiO_3$:Pr^{3+} Nanoparticles. *J. Phys. Chem. C* **2007**, *111*, 18044−18048.
(38) Haranath, D.; Khan, A. F.; Chander, H. Bright Red Luminescence and Energy Transfer of Pr^{3+}-Doped (Ca,Zn)TiO_3 Phosphor for Long Decay Applications. *J. Phys. D: Appl. Phys.* **2006**, *39*, 4956−4960.
(39) Čeh, M.; Kolar, D. Solubility of CaO in $CaTiO_3$. *J. Mater. Sci.* **1994**, *29*, 6295−6300.
(40) Tauc, J.; Menth, A. States in the Gap. *J. Non-Cryst. Solids* **1972**, *8−10*, 569−585.
(41) Katoh, R.; Suzuki, K.; Furube, A.; Kotani, M.; Tokumaru, K. Fluorescence Quantum Yield of Aromatic Hydrocarbon Crystals. *J. Phys. Chem. C* **2009**, *113*, 2961−2965.

DOI: 10.1021/acsomega.7b00761
ACS Omega 2017, 2, 4972−4981